Atmospheric
Measurement
Techniques

Improved rain event detection in commercial microwave link time series via combination with MSG SEVIRI data

Maximilian Graf[1,★]**, Andreas Wagner**[1,★]**, Julius Polz**[2,★]**, Llorenç Lliso**[3]**, José Alberto Lahuerta**[3]**, Harald Kunstmann**[1,2]**, and Christian Chwala**[2]

[1]Institute of Geography (IGUA), University of Augsburg, Alter Postweg 118, 86159 Augsburg, Germany
[2]Campus Alpin (IMK-IFU), Karlsruhe Institute of Technology, Kreuzeckbahnstraße 19,
82467 Garmisch-Partenkirchen, Germany
[3]Agencia Estatal de Meteorología (AEMET Spain), Leonardo Prieto Castro 8, 28040 Madrid, Spain
★These authors contributed equally to this work.

Correspondence: Christian Chwala (christian.chwala@kit.edu)

Abstract. The most reliable areal precipitation estimation is usually generated via combinations of different measurements. Path-averaged rainfall rates can be derived from commercial microwave links (CMLs), where attenuation of the emitted radiation is strongly related to rainfall rate. CMLs can be combined with data from other rainfall measurements or can be used individually. They are available almost worldwide and often represent the only opportunity for ground-based measurement in data-scarce regions. However, deriving rainfall estimates from CML data requires extensive data processing. The separation of the attenuation time series into rainy and dry periods (rain event detection) is the most important step in this processing and has a high impact on the resulting rainfall estimates. In this study, we investigate the suitability of Meteosat Second Generation Spinning Enhanced Visible and InfraRed Imager (MSG SEVIRI) satellite data as an auxiliary-data-based (ADB) rain event detection method. We compare this method with two time-series-based (TSB) rain event detection methods. We used data from 3748 CMLs in Germany for 4 months in the summer of 2021 and data from the two SEVIRI-derived products PC and PC-Ph. We analyzed all rain event detection methods for different rainfall intensities, differences between day and night, and their influence on the performance of rainfall estimates from individual CMLs. The radar product RADKLIM-YW was used for validation. The results showed that both SEVIRI products are promising candidates for ADB rainfall detection, yielding only slightly worse results than the TSB methods, with the main advantage that the ADB method does not rely on extensive validation for different CML datasets. The main uncertainty of all methods was found for light rain. Slightly better results were obtained during the day than at night due to the reduced availability of SEVIRI channels at night. In general, the ADB methods led to improvements for CMLs performing comparatively weakly using TSB methods. Based on these results, combinations of ADB and TSB methods were developed by emphasizing their specific advantages. Compared to basic and advanced TSB methods, these combinations improved the Matthews correlation coefficient of the rain event detection from 0.49 (or 0.51) to 0.59 during the day and from 0.41 (or 0.50) to 0.55 during the night. Additionally, these combinations increased the number of true-positive classifications, especially for light rainfall compared to the TSB methods, and reduced the number of false negatives while only leading to a slight increase in false-positive classifications. Our results show that utilizing MSG SEVIRI data in CML data processing significantly increases the quality of the rain event detection step, in particular for CMLs which are challenging to process with TSB methods. While the improvement is useful even for applications in Germany, we see the main potential of using ADB methods in data-scarce regions like West Africa where extensive validation is not possible.

1   Introduction

Rainfall is the most important variable for hydrology and water management. It is characterized by high variability in space and time, especially in the case of convective rain events. The quality of hydrological modeling results depends heavily on high-resolution and reliable areal rainfall data (Fu et al., 2011; Bruni et al., 2015; Rafieeinasab et al., 2015; Cristiano et al., 2017).

There are a variety of rainfall measurement methods that serve as a basis for the derivation of rainfall fields, each with specific advantages but also drawbacks. Rain gauges can provide point measurements of precipitation with high accuracy, but they are prone to errors due to wind and evaporation (Sevruk, 2006) and primarily lack spatial representativeness (Pollock et al., 2018).

Satellite data provide areal precipitation estimates almost worldwide with a spatial resolution of the order of several kilometers. But they suffer either from a poor temporal resolution like the GPM core satellite that has a revisit time of approximately 1 d in the tropics or from heterogeneous data quality and delayed availability like merged satellite products such as IMERG (Hou et al., 2014). Additionally, complex retrieval and calibration algorithms have to be applied, which cause additional uncertainties (Maggioni et al., 2016).

Weather radars derive areal precipitation estimates with a high resolution of 5 min and 1 km (Atlas, 1990; Bartels et al., 2004; Winterrath et al., 2012). However, the calculation of rain rates from radar reflectivity is non-trivial (Uijlenhoet et al., 2003; Steiner et al., 2004), and false echoes, clutter, and other measurement effects cause further problems (Villarini and Krajewski, 2010; Wagner et al., 2012; Wagner, 2018). Schleiss et al. (2020) showed that radar data tend to underestimate particularly heavy rainfall in Scandinavian countries. Nevertheless, gauge-adjusted radar products are considered to be one of the best possible data basis for spatial rainfall estimates because they leverage the advantages from individual measurement devices (Bartels et al., 2004; Winterrath et al., 2012).

The opportunistic sensing of rainfall with commercial microwave links (CMLs) was first demonstrated in Israel (Messer et al., 2006) and the Netherlands (Leijnse et al., 2007). In recent years CML rainfall estimation has become available on country-wide scales (Overeem et al., 2016; Graf et al., 2020). Rainfall attenuates the microwave radiation between two antennas of a CML. The relationship between attenuation and rainfall is close to linear for signals between 10 and 40 GHz (Atlas and Ulbrich, 1977). CMLs have already proven their potential as stand-alone rainfall sensors in multiple regions of the world (Overeem et al., 2013; Rios Gaona et al., 2015; Overeem et al., 2016; D'Amico et al., 2016; Graf et al., 2020; Roversi et al., 2020; van de Beek et al., 2020; Djibo et al., 2023).

Additionally, the path-averaged rainfall information from CMLs can complement conventional measurement methods (Liberman et al., 2014; Haese et al., 2017; Graf et al., 2021). Kumah et al. (2022), for instance, derived rain intensities from MSG satellite data by a random forest algorithm trained with CML rainfall estimates. For regions with sparse observation networks like most parts of Africa, where radar data are missing and even station data are only sparsely available, CMLs can deliver additional ground-based rainfall estimates (Djibo et al., 2023). Thus, the use of CML data is a good opportunity to reduce the gap in the global availability of climate information, as recently emphasized by UNFCCC (2022).

The detection of rain events in CML attenuation time series is an important processing step for several reasons. First, it defines the rainy periods for which a baseline has to be defined, typically from preceding dry time steps. Second, it filters fluctuations that are not caused by rain but by other disturbances, e.g., from refraction, multi-path propagation, or mast sway (see Chwala and Kunstmann, 2019 for a detailed list). For an overview of available rain event detection methods, we divide them into two categories: time-series-based (TSB) methods and methods based on auxiliary data of rainfall patterns (ADB). ADB methods that are based on globally available data like the satellite data presented in this study are especially promising for CML processing in regions with otherwise sparse rainfall information.

Examples of TSB methods are the simple threshold models (Leijnse et al., 2008), an approach using the rolling standard deviation (Schleiss and Berne, 2010), Markov switching models (Wang et al., 2012), or short-term Fourier transform approaches (Chwala et al., 2012). Messer and Sendik (2015) provide a detailed description of these approaches. Machine learning approaches to distinguish between wet and dry time steps emerged in recent years, usually outperforming the previous methods (Habi and Messer, 2018; Polz et al., 2020; Song et al., 2020). The "nearby-link" approach (Overeem et al., 2016) is a hybrid TSB and ADB method because it compares CML attenuation time series of neighboring CMLs. Similar to CMLs, satellite microwave links (SMLs) can be exploited to derive rainfall estimates. SML processing also includes rain event detection and several methods are available (Giannetti et al., 2019; Giro et al., 2022).

Data sources in ADB methods can be weather radar (Overeem et al., 2011) or satellite data (van het Schip et al., 2017; Kumah et al., 2021). Regarding satellite data, geostationary satellites such as MSG SEVIRI offer a temporal resolution of 15 min at 4×6 km spatial resolution in midlatitudes. These data are also used as areal precipitation (Roebeling et al., 2008; Roebeling and Holleman, 2009), although the derivation of precipitation from Vis and IR channels is often uncertain. According to NWC SAF (Lahuerta García, 2021), even a distinction between light, moderate, and heavy precipitation is difficult. That is why they determine the probability of precipitation in their post-processed SEVIRI products.

The study by van het Schip et al. (2017) analyzed applying post-processed SEVIRI products as a wet–dry indicator in the Netherlands. They evaluated the resulting rainfall maps for 12 d and found improvements compared to not separating the time series into wet and dry periods but a decreased performance compared to radar-based rain event detection. However, they did not compare the methods for individual CMLs, different rainfall intensities, or day and night periods for which the satellite products use different channels and methodologies. They also did not combine their ADB method with a TSB method.

Kumah et al. (2021) obtained improved rain intensities for convective rain events when applying MSG SEVIRI data for rain event detection of CML data. However, their results are based only on one CML in Kenya for daytime and for rain intensities above $0.5 \, \mathrm{mm \, h^{-1}}$. The limitation of both studies regarding the analyzed period, the number of CMLs, intensity classes, and day and night differences hinders the transferability of their results. None of the rain event detection methods presented can provide a high-quality classification for CML datasets with varying characteristics (e.g., sparse or dense network, various temporal resolutions, different frequency ranges). CMLs with frequencies below 10 GHz which are commonly deployed in sparse CML networks in rural sub-Saharan Africa still pose great challenges for all available rain event detection methods. Yet, these regions are often associated with a high potential for CML as the sole source of rainfall estimates.

In this study, the precipitation products PC (Precipitating Clouds) and PC-Ph (Precipitation Clouds from Cloud Physical Properties), which are computed by NWC SAF using data from the SEVIRI radiometer on board the geostationary satellite METEOSAT, are used to classify CML attenuation time series in rainy and dry periods. In addition to comparing ADB (based on PC and PC-Ph) and TSB (CML time series processing) methods, this study presents a novel way of combining TSB and ADB rain event detection approaches to improve rain event detection. To analyze the applicability of such new rain event detection methods, datasets of high data quality are necessary. The present analysis is based on country-wide CML data from 4 months in the summer of 2021 in Germany. As a reference, a high-resolution gauge-adjusted radar product is used.

The research questions of this investigation are as follows: (1) are PC and PC-Ph products suitable as wet–dry indicators for CML data? (2) Do the results vary with rain intensity? (3) Are there noticeable differences between day and night? (4) Can a combination of TSB and ADB rain event detection methods outperform TSB-only and ADB-only methods?

2 Data

This study is based on CML, weather radar, and SEVIRI data in Germany covering the period from 30 April 2021 to
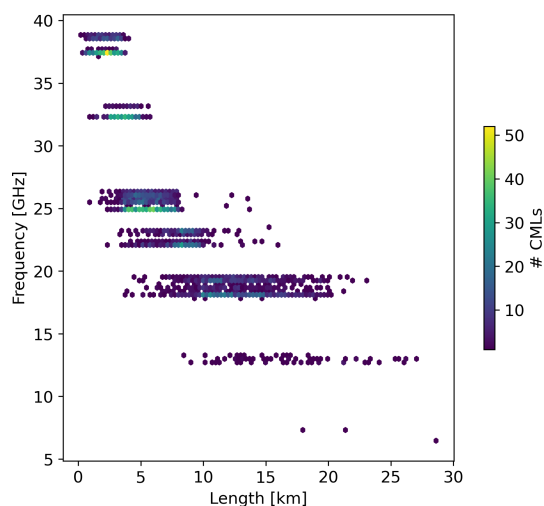

Figure 1. Scatter density plot showing the distribution of length and frequency of the 3748 CMLs in Germany that are used in this study.

10 September 2021. Table 1 summarizes the properties of these products.

2.1 CML data

The CML dataset consists of a subset of CMLs operated by Ericsson in Germany. For the period analyzed, 3748 CMLs were available for more than 30 % of the time and thus considered in this study. The path length of the CMLs varies between 0.2 km and about 30 km, and the frequencies range from 10 to 40 GHz, with shorter CMLs using higher frequencies (see Fig. 1). The transmitted signal level (TSL) with a power resolution of 1 dB and the received signal level (RSL) with a power resolution of 0.3 dB are instantaneously measured every minute using a custom real-time CML data acquisition system (Chwala et al., 2016). The total loss (TL) is the difference between TSL and RSL. Each CML consists of two sublinks for two-way data transmission. The processing of the data is described in Sect. 3.2.

2.2 Weather radar data

RADKLIM-YW is a gauge-adjusted, climatologically corrected radar product of the German Meteorological Service (DWD). The hourly adjustment with data from automatic rainfall stations is identical to that of the RADOLAN-RW product (Bartels et al., 2004; Winterrath et al., 2012). Daily sums are adjusted with daily measurements of manual rainfall stations and climatology-based corrections of spokes and range dependencies are carried out (Winterrath et al., 2018). RADKLIM-YW data have a temporal resolution of 5 min and a spatial resolution of 1 km covering Germany with 1100×900 grid cells. According to Kreklow et al. (2020), the range-dependent effects, which are particularly strong in winter, are reduced. This improves rainfall patterns and bet-

Table 1. Overview of rainfall sensors and products.

Sensor	Product	Spatial resolution (longitude × latitude)	Temporal resolution	Data points (including missing values)
C-band weather radar	RADKLIM-YW	1 km × 1 km	5 min	30 808 350 000
MSG SEVIRI	PC & PC-Ph	3.4–5.1 km × 4.0–6.4 km	15 min	1 330 560 000
CML	–	3748 CML paths	1 min	765 649 270

ter represents orography compared to RADOLAN-RW. At the same time, however, a slight underestimation of the total rainfall was determined.

RADKLIM-YW is used to validate the binary classifications of rain event detection methods and the rainfall estimates derived from CMLs using these methods. To compare the gridded RADKLIM-YW with the CMLs, we averaged the grid for each individual CML path weighted by the length of intersecting path segments in each pixel. RADKLIM-YW was aggregated to a resolution of 15 min. For the usage as a binary wet–dry reference, we used a rainfall intensity threshold of $0.1\,\mathrm{mm\,h^{-1}}$ at the 15 min resolution. All values below $0.1\,\mathrm{mm\,h^{-1}}$ were considered dry.

To answer research question (2), on whether the performance of rain event detection methods shows a rain rate dependency, we define intensity classes and group the 15 min radar rainfall intensities. The classes light $(0.1–2.5\,\mathrm{mm\,h^{-1}})$, moderate $(2.5–10.0\,\mathrm{mm\,h^{-1}})$, and heavy (more than $10.0\,\mathrm{mm\,h^{-1}}$) rainfall are based on the DWD (2023a) classification. Light rainfall is further subdivided into the classes light1 $(0.1–1.0\,\mathrm{mm\,h^{-1}})$ and light2 $(1.0–2.5\,\mathrm{mm\,h^{-1}})$. Values below $0.1\,\mathrm{mm\,h^{-1}}$ are considered dry. The resulting classes are shown in Fig. 7.

2.3 SEVIRI data

The Spinning Enhanced Visible and Infrared Imager (SEVIRI) radiometer from the geostationary satellite METEOSAT provides image data in two visible (Vis), one high-resolution Vis, and nine infrared (IR) channels including one near-infrared channel (NIR). The channels range from 0.5 to $14.4\,\mu\mathrm{m}$ with a resolution of 3 km at the sub-satellite point. The high-resolution channel is not used for our purposes. Every 15 min a calibrated image of the full Earth disk (lat -81 to $81°$, long -79 to $79°$) is available (Schmid, 2000). No spaceborne radar or radiometer for precipitation measurement is on board, such as for GPM (Hou et al., 2014). Precipitation products are derived based on two approaches: either by regression of different channels and adjustment to precipitation measurements or, more sophisticatedly, by deriving microphysical parameters (Roebeling et al., 2008; Hernanz et al., 2019). For the calculation of microphysical parameters, the $0.6\,\mu\mathrm{m}$ channel (Vis) and the $1.6\,\mu\mathrm{m}$ channel (NIR) are mandatory (Roebeling et al., 2008).

The first product, PC-Ph, is derived from the microphysical parameter effective radius (Reff) and cloud optical thickness (COT) during daytime. At night, when visible channels are missing, it is calculated by a regression of IR and water vapor (WV) channels. The second product, PC, relies on different regression functions of available SEVIRI channels, including Vis, IR, and WV channels during daytime and only IR and WV channels at night. The definition of daytime and nighttime is derived from the variable pccond that is provided for both PC and PC-Ph. Both products are provided by NWC SAF. Recent data are freely available, but long-term records must be requested individually.

We chose both products for this study because they provide the probability of precipitation in percent: PC in increments of 10 and PC-Ph in increments of 1 %. Compared to a pure precipitation product, the precipitation probability products enabled us to consistently alter the classification threshold similar to how it can be done for certain TSB methods. Example time series of the precipitation probability are shown in Fig. 2b and c. More detailed descriptions and the evaluation of the two products are available from Thoss (2014), Hernanz et al. (2019), and Lahuerta García (2019). Similar to RADKLIM-YW, we derived PC and PC-Ph values along the CML paths. The validation of PC or PC-Ph wet and dry labels is based on the path averages of RADKLIM-YW.

3 Methods

3.1 Rain event detection

3.1.1 Individual methods for rain event detection

We used two existing time-series-based (TSB) methods as a baseline for rain event detection. The first one is based on the rolling standard deviation of total loss (TL). Time steps for which the standard deviation of a 60 min rolling window exceeds a certain threshold are considered wet. This approach was originally suggested by Schleiss and Berne (2010), who used a fixed threshold. Later, Graf et al. (2020) determined the threshold based on the 80th percentile of the 60 min rolling standard deviation of TL multiplied by a scaling factor of 1.12 that adapted the threshold to the general amount of noisiness of each CML. This method will be called RS. The second method is a machine learning approach based on a convolutional neural network (CNN) that was trained to classify TL time series into rainy and dry time steps from Polz et al. (2020). This model provides a continuous probability
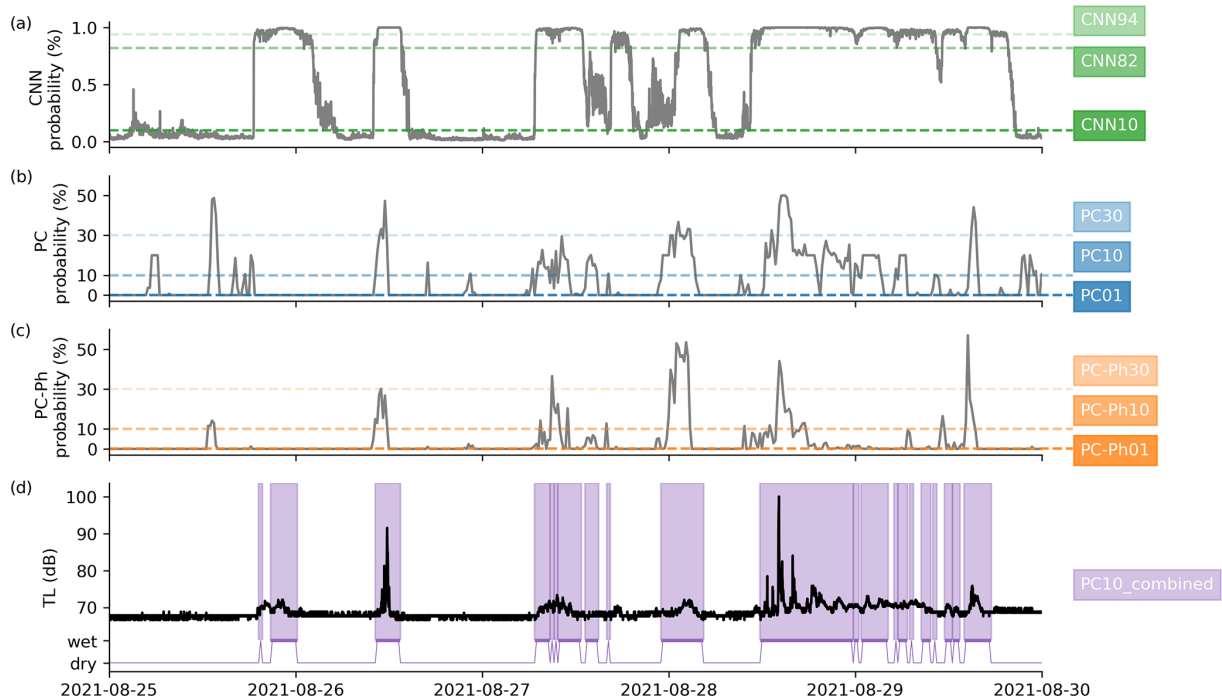
Figure 2. Example time series of 5 d showing the probability of rainy time steps from **(a)** convolutional neural network (CNN), **(b)** PC, and **(c)** PC-Ph for the total loss (TL) time series in **(d)**. The dashed lines in **(a)**, **(b)**, and **(c)** represent the thresholds that separate the probabilities into rainy and dry time steps. Higher thresholds (CNN94, PC30, PC-Ph30) lead to a conservative rain event detection, classifying only time steps as rainy which have a high probability of being rainy; in contrast, low thresholds (CNN10, PC10, PC-Ph01) lead to a liberal rain event detection, and only time steps that are very likely dry are dry. Additionally, the combination of PC10 with CNN and PC variants as rain event detection methods is shown in **(d)**.

between 0 and 1 that describes the likeliness that a time step is rainy. Therefore, the choice of threshold that divides the probability values into rainy and dry time steps determines whether the classification is more liberal or conservative. We adopted the classification threshold of 0.82, which was found to be optimal by Polz et al. (2020). This method will be called "CNN". Figure 2a shows an example of the CNN probability and the three thresholds used later in the combination of rain event detection methods. Both TSB approaches were compared in Polz et al. (2020) based on hourly data with a significantly better performance of CNN compared to RS. Identically to Polz et al. (2020), we computed RS and CNN based on 1 min TL data.

We used PC and PC-Ph products from SEVIRI data as ADB rain event detection by applying a threshold on their precipitation probabilities. We used the thresholds 30 %, 20 %, 10 %, and 0.1 %. The last threshold represents probabilities greater than 0 %. The abbreviations for the thresholds are, e.g., P30 or P01, and the abbreviations for the specific data sets of PC and PC-Ph are, e.g., PC10 or PC-Ph10. We forward-filled the 15 min classification to a 1 min resolution in the CML processing described in Sect. 3.2. This temporal resolution is necessary for the two TSB methods and other CML processing methods such as WAA compensation and

baseline estimation as they were developed and tested for this resolution (Graf et al., 2020).

3.1.2 Combinations of rain event detection methods

The main goal of this study is to improve rain event detection compared to already available methods by combining TSB and ADB methods. Using TSB methods, detecting light rain events is more difficult than detecting strong rain events because it is harder to differentiate smaller attenuation from fluctuations induced by other factors than rain. ADB methods do not use TL for rain event detection, overcoming this issue, but in the case of SEVIRI, uncertainties are introduced by the indirect measurement principle and the difficulties of separating light rain from no rain. We therefore propose combining TSB and ADB methods to exploit their advantages. We use different probability thresholds for CNN and the two SEVIRI products to derive rain event detection variants with either high confidence in the correct classification of rainy time steps or high confidence regarding dry time steps. The thresholds used are shown in Fig. 2. CNN10 and PC01 are liberal variants in the sense that they classify rainy time steps already for low probabilities, potentially introducing many false positives (FPs). Hence, time steps that are predicted to be dry have a lower chance of being false negative (FN). In

contrast, CNN94 and PC30 are considered conservative variants because they only classify time steps with a very high probability as rainy. This leads to a low number of FPs while introducing more FNs.

Our procedure of combining the rain event detection variants consists of five individual steps presented in Fig. 3 and algorithm 1 shown in Fig. A1. We combined either CNN and PC or CNN and PC-Ph. In the following, the combination of CNN and PC is explained. In step 1, we choose a method with an intermediate threshold as a starting point which is either CNN82, PC01, or PC10. Step 2 uses the dry time steps from the liberal variant PC10 (even if it was used as the starting point) that has a high confidence for dry time steps to replace rainy time steps from step 1. Steps 3 and 4 use time steps with high confidence of being rainy from CNN94 and PC30 to replace time steps classified as dry after step 2. In step 5, dry time steps from CNN10 are used to replace previously rainy time steps. The combination of CNN and PC-Ph is identical using PC-Ph with the same thresholds instead of PC. The results of six combinations are shown in Fig. 5. We named the combinations based on their initial product used for step 1 as the other steps were identical for each combination, e.g., PC10-combined.

In total, we will evaluate two TSB methods (RS and CNN), eight ADB methods (derived from the two SEVIRI products PC and PC-Ph with four thresholds, respectively), and six combinations of TSB and ADB methods.

3.2 CML data processing

Deriving rainfall estimates from CMLs is a delicate matter (Uijlenhoet et al., 2018). Various research groups developed individual CML processing methods that depend on, e.g., the sampling strategy of data. The most important aspects of data processing are briefly outlined hereafter, while a more detailed description of the processing steps can be found in Graf et al. (2020). We removed default values and outliers that were outside the range $[-10, 40]$ dB for TSL and $[-99, 0]$ dB for RSL from the analysis. The total path loss along the CML (TL) was then calculated as TSL minus RSL. We interpolated gaps in TL time series of up to 5 min to obtain a more continuous data availability.

For the rain event detection, we used two TSB methods, two ADB methods with four different thresholds, and six combinations of TSB and ADB methods. As SEVIRI is only available with a 15 min resolution, we resampled their classification to a 1 min resolution with a forward-fill. We computed the following processing steps for each rain event detection method on a 1 min basis to derive individual rainfall estimates. The baseline attenuation was dynamically identified from the preceding dry period of each rain event to derive the rainfall-induced attenuation along the path. The baseline was determined by the last dry time step of the TL time series and was set to be constant during the rain event. As water on the CML antenna covers can lead to additional attenuation,

this so-called wet antenna attenuation (WAA) effect has to be compensated for. We used the WAA correction from Leijnse et al. (2008). In this physical approach, the WAA depends on antenna cover properties (refractive index and thickness), microwave frequency, and rain intensity. We used the parameters given by Leijnse et al. (2008). The rainfall rate was derived from WAA-corrected attenuation using the k–R relation. The parameter settings for the k–R relation were taken from ITU recommendations (ITU-R, 2005). From a purely practical point of view, we only evaluated data from the first of the two available sublinks.

For comparison with the reference, the binary classifications from the TSB methods and all resulting rain rates were resampled to a 15 min resolution. We believe that a resampling to 15 min and the fact that RADKLIM-YW is adjusted to rain gauges suffice for overcoming the potential temporal mismatch between radar- and ground-based CML observations. The evaluation with a 15 min resolution might lead to worse results than one on an hourly basis. But for future applications of SEVIRI products for CML processing in regions with sparse reference data like sub-Saharan Africa, this high temporal resolution is advantageous.

3.3 Statistical measures

The radar rainfall estimates at a 15 min resolution serve as the ground truth for the computation of the scores listed below. For binary classification scores, the ground truth is considered wet if the path-averaged radar rain rate (r_{ref}) along the CML path is larger than 0.1 mm h^{-1}. The Pearson correlation coefficient (PCC) is used to evaluate the quality, in terms of the linear correlation, of different CML rainfall estimates (r_{cml}) derived by using the proposed methods for rain event detection:

$$\text{PCC} = \frac{\sum (r_{ref} - \overline{r_{ref}}) (r_{cml} - \overline{r_{cml}})}{\sqrt{\sum (r_{ref} - \overline{r_{ref}})^2}\sqrt{\sum (r_{cml} - \overline{r_{cml}})^2}}, \quad (1)$$

where the $\overline{r}$ indicates the mean of a quantity. The relative bias (RB) is then used to measure an over- or underestimation that cannot be derived from the PCC:

$$\text{RB} = \frac{\sum (r_{cml} - r_{ref})}{\sum r_{ref}}. \quad (2)$$

Binary classification scores are based on the confusion matrix:

$$\begin{pmatrix} \text{TP} & \text{FP} \\ \text{FN} & \text{TN} \end{pmatrix} = \begin{pmatrix} \text{WET/wet} & \text{DRY/wet} \\ \text{WET/dry} & \text{DRY/dry} \end{pmatrix}, \quad (3)$$

with uppercase and lowercase denoting observed events and predictions, respectively. The correctly assigned wet time steps are called "true positives" (TPs) and the correctly assigned dry times steps are "true negatives" (TNs). False positives (FPs) represent the number of time steps where rain event detections are incorrectly assigned wet time steps, and
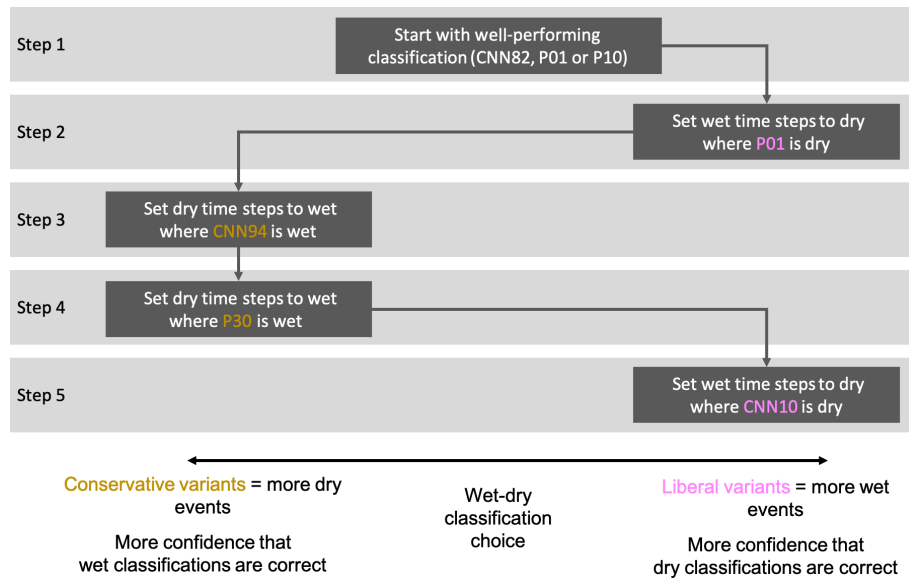
Figure 3. Flowchart for building a combination based on TSB and ADB rain event detection methods This stepwise approach starts with an already well-performing classification as a starting point. Then, during each step, time steps that have a high likelihood of being dry (or we) from a very liberal (or conservative) classification from the two methods used are added to the previous classification. If PC is used as a starting point, steps 2 and 4 also use PC. The same is true for PC-Ph. For CNN82 as a starting point, we computed one variant with PC and one with PC-Ph. An algorithmic description of this flowchart can be found in Fig. A1.

false negatives (FNs) represent the number of incorrect dry time steps. The confusion matrix fully explains the performance of a classifier, but since the interpretation of four individual numbers is not straightforward, the computation of additional scores is necessary. The first simplification is to reduce it to the pair of true-positive rate (TPR, Eq. 4), which is the probability of a positive event being predicted positive, and the false-positive rate (FPR, Eq. 5), also called the "false-alarm rate". We include both scores since the importance of a high TPR or FPR may be weighted differently depending on the application of the CML rainfall rates.

$$\text{TPR} = \frac{\text{TP}}{(\text{TP} + \text{FN})} \quad (4)$$

$$\text{FPR} = \frac{\text{FP}}{(\text{FP} + \text{TN})} \quad (5)$$

In this paper, we focus on improving the overall performance of rain event detection and thus use the Matthews correlation coefficient (MCC, Eq. 6), which is more robust to influences of the skewed distribution of wet and dry classes (the ratio is roughly $1:20$). The MCC is high only if the detection performance for both wet and dry classes is high.

$$\text{MCC} = \frac{(\text{TP} \cdot \text{TN} - \text{FP} \cdot \text{FN})}{\sqrt{(\text{TP} + \text{FP})(\text{TP} + \text{FN})(\text{TN} + \text{FP})(\text{TN} + \text{FN})}} \quad (6)$$

The classifier accuracy (ACC, Eq. 7) is used to analyze the performance for the different rainfall intensity classes and gives the percentage of the time steps in the intensity class

that were detected as wet (or dry for the dry class).

$$\text{ACC} = \frac{(\text{TP} + \text{TN})}{(\text{TP} + \text{FP} + \text{FN} + \text{TN})} \quad (7)$$

4 Results

In this section, we first compare the ADB products derived from Meteosat-SEVIRI with the weather radar reference to assess their suitability as wet–dry indicators within the processing of CML data. Subsequently, we analyze the relative performance of ADB and the combination of ADB and TSB methods with respect to the performance of established TSB methods. Then, we analyze the performance regarding different rain intensity classes and investigate the influence of different rain event detection methods on the performance of individual CMLs. All the rain event detection methods presented here were used in combination with the CML processing routine described in Sect. 3.2, and the resulting datasets were compared with the path-averaged weather radar reference on a 15 min basis. All scores computed for all methods and the full dataset are additionally shown in the Appendix (see Table B1).

4.1 Rain event detection performance of the PC and PC-Ph SEVIRI product

To assess the quality of the SEVIRI products, they can be compared directly to the weather radar reference. To overcome the issue of their different grid sizes and to assess their

quality for their use in CML processing, we compared SE-VIRI and RADKLIM-YW data as path averages along the CML paths. To compare the PCC of the different SEVIRI-based products and the applied thresholds, processing the CML rainfall rates according to Sect. 3.2 was performed using the SEVIRI wet–dry indicator.

Figure 4 compares the performance of the PC and PC-Ph products according to the TPR, FPR, MCC, and PCC scores. The highest TPR (0.83 during the day and 0.9 during the night) was achieved by the lowest threshold for PC and PC-Ph (P01), which also showed the highest FPR (0.14 during the day and 0.22 during the night). For PC, the TPR and FPR were increased during the night, but for PC-Ph, only the FPR was significantly increased during the night, except for the P30 version which also showed a higher nighttime TPR. Both the TPR and FPR decreased with increasing threshold, which is due to the decreasing number of positive predictions. The ratio of TP + FP and TP + FN describes how many more time steps a method predicted as wet compared to the reference. Accordingly, PC01 showed 195 % (151 % for PC-Ph01) more wet time steps than the radar data, and PC30 showed the opposite behavior with 36 % (52 % for PC-Ph30) fewer wet time steps than the reference (see Table B1 in the Appendix).

The MCC shown in Fig. 4, which measures the overall classification performance, showed that the P10 threshold yields the best results for PC during the day and night. The best results for PC-Ph were achieved by the P10 threshold during daytime and by the P01 threshold during nighttime.

Figure 7b shows the accuracy of PC and PC-Ph. The accuracy increases with a higher threshold, whereas the relative bias shown in Fig. 7d becomes more negative with higher absolute values, suggesting an increasing underestimation compared to the radar. This is due to an increasing number of TN and FN predictions.

When computing CML rainfall rates based on the PC and PC-Ph wet–dry labels, the highest PCC was achieved using the P01 threshold with values around 0.72. P10 showed only marginally lower scores. When higher thresholds were applied, the performance decreased more severely. Overall, PC showed slightly higher scores than PC-Ph and the performance during daytime was equal to or better than the performance at nighttime.

According to this analysis, P01 and P10 were the most promising thresholds to apply for SEVIRI-based, pure ADB wet–dry detection. Both PC and PC-Ph show good classification and regression scores for these thresholds. Because of the bad PCC, P30 is not suitable as a threshold for a stand-alone ADB method and we did not analyze its performance any further. However, we did use it for wet labels with high confidence in the combination algorithm.

4.2 Comparison of ADB (PC and PC-Ph), TSB, and combined rain event detection methods

Due to the increased number of products that are evaluated in this subsection, we limit the analysis to using only the MCC as a measure of classification performance since it gives the best summary of the confusion matrix in one scalar value. Figure 5 shows an analysis that was carried out for the two TSB methods RS (gray) and CNN (green) and for six ADB methods using the three lowest thresholds (0.1, 10, and 20) of PC (blue) and PC-Ph (orange). The SEVIRI products, PC and PC-Ph, performed similarly well to the CNN and RS methods during daytime, with MCC scores ranging from 0.49 to 0.51. The best performance during daytime was achieved by PC-Ph10 and the worst by PC-Ph20. During nighttime, the CNN outperformed the ADB methods, while the standard deviation approach showed a similar performance to PC and PC-Ph except for the higher P20 threshold, which showed the worst performance. Probabilities of 20 % and above (not shown here) showed even worse results.

At night, the results of RS were worse than during the day. One reason could be dew formation on the CML antenna cover, causing an increasing signal attenuation resulting in increased standard deviation, which leads to false classification as wet. The CNN did not show differences between day and night, suggesting that it coped better with this issue. The SEVIRI-based products also showed slightly worse results during nighttime, but this was most likely due to the lack of three SEVIRI channels in the Vis and NIR at night.

SEVIRI-based rain event detection with probabilities of up to 10 % provided a similar performance to RS and CNN during the daytime but performed worse than CNN during the night.

Figure 6 shows an example time series of TL, TP, FP, and FN classifications and the rainfall rate of the PC10 and CNN methods as well as the combined method PC10-combined. It can be seen that the choice of rain event detection method has an impact on the resulting rainfall rate. The combined method improves the classification performance and correlation of rainfall rates compared to the pure ADB and TSB methods.

In addition to the individual TSB and ADB methods, Fig. 5 shows six different combined methods (purple and red) that are composed of CNN, PC01, or PC10 as a starting point and done for either PC or PC-Ph. As before, PC is shown on the left and PC-Ph on the right.

The main difference among the combinations is that PC data performed better than PC-Ph during daytime and similar at nighttime. CNN and PC(-Ph)10 were the best-performing TSB and ADB methods and were, therefore, compared with the combined products. PC10-combined showed the largest overall improvements with an MCC of 0.59 compared to 0.52 (CNN) and 0.52 (PC-Ph10) during daytime and 0.55 compared to 0.50 (CNN) and 0.41 (PC10) at nighttime. PC10-combined also showed the lowest relative bias of
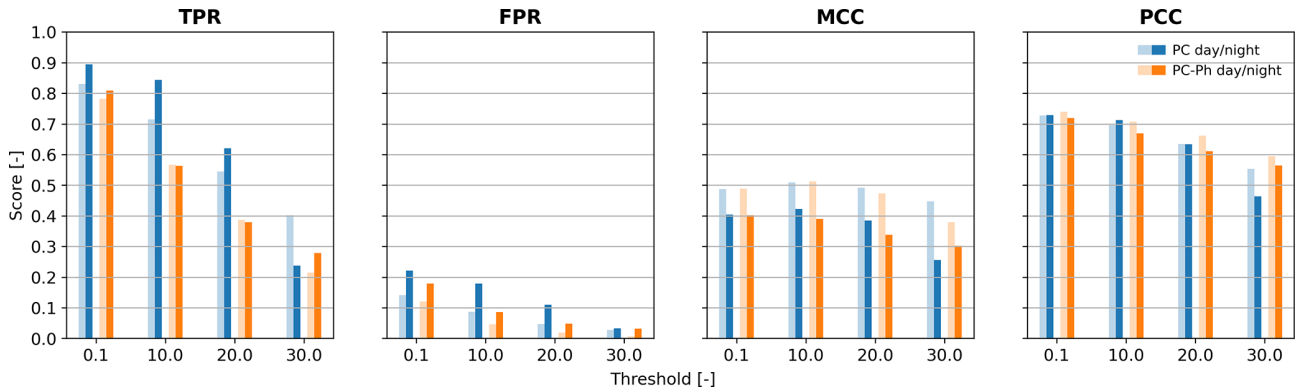
Figure 4. Performance metrics of the binary rain event classification (TPR, FPR, and MCC) and the rainfall rates (PCC) of the PC (blue) and PC-Ph (orange) products compared to the radar reference. The results of each score are presented for different thresholds (*x* axes) and split into day (light colors) and night (dark colors).
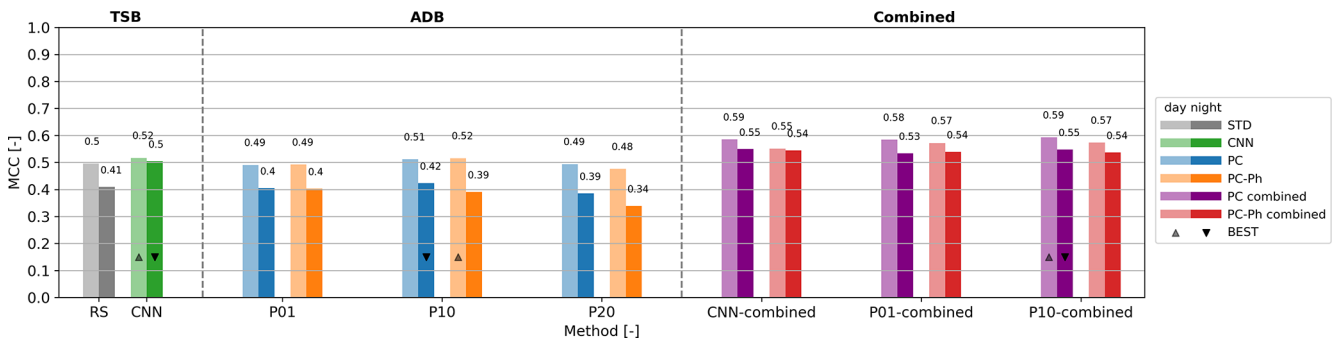

Figure 5. Matthews correlation coefficient (MCC) of pure TSB, ADB, and combined methods. P01, P10, and P20 refer to the respective PC and PC-Ph thresholds. The results are split into day (light colors) and night (dark colors). The best-performing day and night products of each group are marked with a triangle.

−2.1 % compared to PC01-combined with 2.6 % and CNN-combined with −10.8 % (see Fig. 4d). The relative bias was also lower than that of pure TSB or ADB methods. In the following, we concentrate on PC10-combined to evaluate the performance gain using a combination of ADB and TSB methods in more depth for different intensity classes and individual CMLs.

PC10 showed the best performance when combined with the CNN method (described and shown in the next section) and is thus used as a new ADB method for all final results in the following sections.

4.3 Performance of rain event detection methods for different rain intensity classes

Figure 7 shows the accuracy and relative bias for the TSB, ADB, and combined methods. The relative bias is, for all individual intensity classes, a percentage of the average reference rainfall rate (mean over all classes) such that Fig. 7c is the sum of the classes shown in Fig. 7d.

It can be observed that for all methods the accuracy increased with increasing intensity and that the CNN per-

formed better than RS for all intensities, which confirms the results of Polz et al. (2020) for the same CML network but a different period. Therefore, we omit RS in the remaining Results section. Overall, all rain event detection methods lead to an underestimation of light to heavy rainfall, which was only partly compensated for by an overestimation from FPs (dry class).

PC performed better than PC-Ph for light to moderate intensity and similar for heavy intensity but had a lower accuracy for the dry class, suggesting more FPs for PC when the same threshold was chosen.

Although more methods are shown, we will focus on the best TSB (CNN), ADB (PC10), and combined (PC10-combined) methods from here on to sharpen the analysis.

For the lowest class, light1, we observed large differences in accuracy with 60.1 % (CNN), 73.2 % (PC10), and 77.8 % (PC10-combined), while the accuracy was similar for the highest class, heavy, with 93.7 % (CNN), 91.0 % (PC10), and 94.3 % (PC10-combined). The TSB and combined methods showed a similar dry accuracy, which was higher than for the ADB methods.
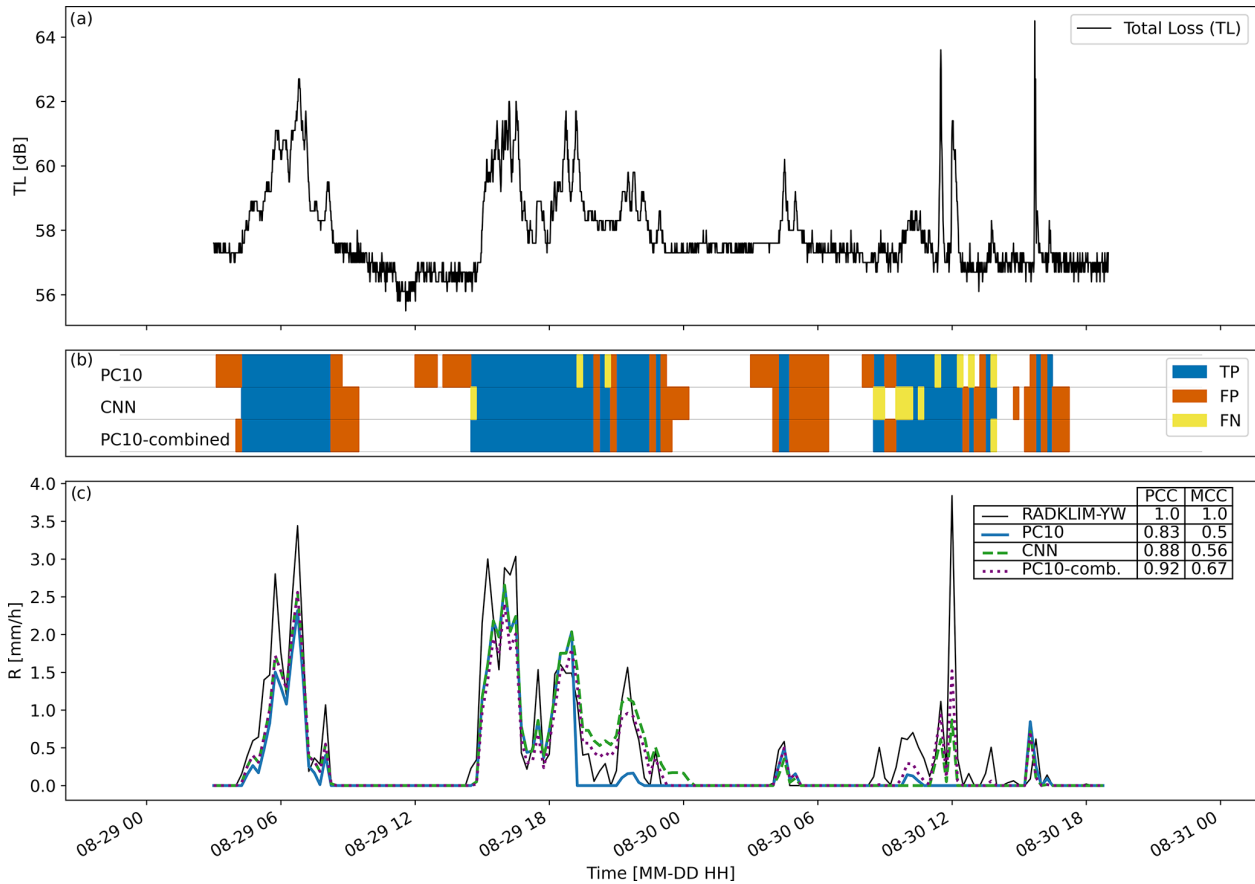
Figure 6. Example time series of total loss (TL) **(a)**, classifications compared to the reference **(b)**, and rainfall rates **(c)**. The scores provided in **(c)** are computed for data from the CML and the period shown in this figure.
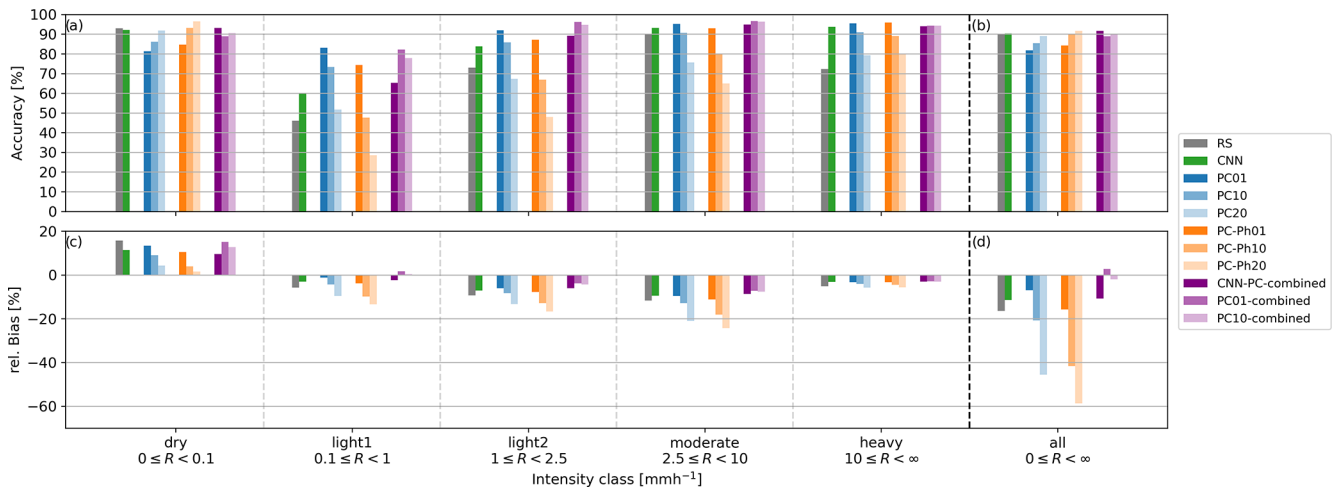

Figure 7. Accuracy **(a, b)** and relative bias **(c, d)** of selected TSB, ADB, and combined methods (see legend). Both scores are shown for different intensity classes (*x* axis) as defined by the radar reference. The accuracy is the percentage of correctly detected rain events in this intensity class. The relative bias in each class is the sum of all errors in one class as a percentage of the total rainfall of the full reference data. This way, the five leftmost classes add up to the "all" class in **(d)**.

The positive relative bias due to FPs (Fig. 7c dry class) is similar for CNN (11.3 %), PC10 (8.9 %), and PC10-combined (12.7 %). The relative bias for the light, moderate, and heavy classes is negative (underestimation) for all methods but has a smaller absolute value for PC10-combined. For example, the bias for the light2 class is −7.1 % (CNN), −8.4 % (PC10), and −4.4 % (PC10-combined). Overall, PC10-combined (−2.1 %) shows a much lower bias than the TSB and ADB methods of CNN (−11.5 %) and PC10 (−20.8 %).

Figure 8 shows histograms of the occurrence and accumulated rainfall amount of CNN, PC10, and PC10-combined using logarithmic bin widths to be able to visualize differences for all intensity classes. PC10-combined showed the highest count of TPs and the lowest count of FNs. Despite this, the number of FPs was lower than for PC10. PC10 showed a similar TP count as CNN but also has the highest number of FPs. The CNN was the most conservative method with the lowest number of FPs. The average rainfall amount per count per CML was different for TPs and FPs. TPs occurred for higher rainfall rates, and therefore this average was 0.43 mm (CNN), 0.39 mm (PC10), and 0.40 mm (PC10-combined). FPs occurred for lower rainfall rates, and therefore the average was 0.09 mm (CNN and PC10 combined) and 0.07 mm (PC10). The average missed rainfall per FN, as measured by the radar reference, was 0.16 mm (CNN), 0.21 mm (PC10), and 0.15 mm (PC10-combined).

To analyze the confidence of individual methods for light, moderate, and heavy rainfall predictions, we computed the probability of a positive prediction coinciding with the reference (i.e., the ratio $\frac{TP}{TP+FP}$). For the light1 class, PC10-combined was the most confident method with 0.56 compared to 0.55 and 0.53 (CNN and PC10). For the light2 and moderate classes, PC10 was the most confident and CNN was the least confident method. For the heavy class, CNN was the most confident and PC10-combined was the least confident method.

4.4 Influence of chosen rain event detection method on individual CMLs

The results so far were based on metrics that we computed using all CML data. The performance of individual CMLs might, however, differ from this mean behavior, and systematic differences between CMLs that compare well or badly with the reference are possible. Therefore, scatterplots of the MCC and PCC calculated for each CML individually are shown to compare CNN and PC10 with PC10-combined in Fig. 9. For the majority of CMLs, the MCC and PCC could be improved by using PC10-combined instead of the best TSB (CNN) and ADB (PC10) method. The average of the MCCs using PC10 (or CNN) was increased from 0.44 (or 0.51) to 0.56. The CMLs with the worst MCC from CNN were improved most when using the combination. For PCC the improvement was smaller (from 0.75 (0.78) to 0.79) but still af-

fected more than 80 % of all CMLs. While PC10-combined, compared to PC10, improved the PCC by up to 0.36 for individual CMLs, the largest improvement from CNN to PC10-combined was 0.15. CMLs with the worst PCC could not be improved by using PC10-combined.

Compared to the overall PCCs of PC10, CNN, and PC10-combined shown in Table B1, the mean of all CML PCCs is slightly higher for all three products. This means that individual CMLs have a higher linear correlation with the reference than the full dataset. Therefore, one can assume that individual CMLs show different biases that could not be compensated for by any of the methods.

5 Discussion

5.1 Suitability of PC and PC-Ph products as wet–dry indicators for CML data

The performance of PC and PC-Ph as wet–dry indicators for CML data was analyzed in Sect. 4.1 and compared with TSB methods in Sect. 4.2. The results showed that the classification scores were only slightly lower than for the TSB methods. In general, the probability threshold had a larger influence on the rain event detection than the differences between PC and PC-Ph. Both products showed better performance for smaller probability thresholds. The linear correlation (PCC) of derived CML rainfall rates with the reference was highest when the threshold was lowest, which is due to the lower impact of FPs on PCC compared to FNs. This is surprising because a more liberal classification than using PC01 was not possible. Usually, extremely liberal or conservative methods are assumed to perform badly, which was the case for conservative thresholds P20 and higher. For the SEVIRI products, this does not seem to be the case. One reason might be that the cloud mask, which both products use, has a good performance over Europe and therefore has a high probability of true-dry detection, resulting in a low number of FPs in general and thus also for low thresholds.

In summary, PC and PC-Ph products perform surprisingly well as wet–dry indicators for CML data. Since these ADB methods are independent of the CML data, they can significantly improve the rain event detection step for noisy CMLs where erratic fluctuations hamper TSB methods. One limitation of the approach based on SEVIRI data is that the temporal resolution can be more than 1 magnitude lower than the resolution of the CML data (e.g., 15 min vs. 1 min). However, the recently launched Meteosat Third Generation (MTG) satellites with the Flexible Combined Imager (FCI) will improve the temporal resolution from 15 min of MSG SEVIRI to 10 min.
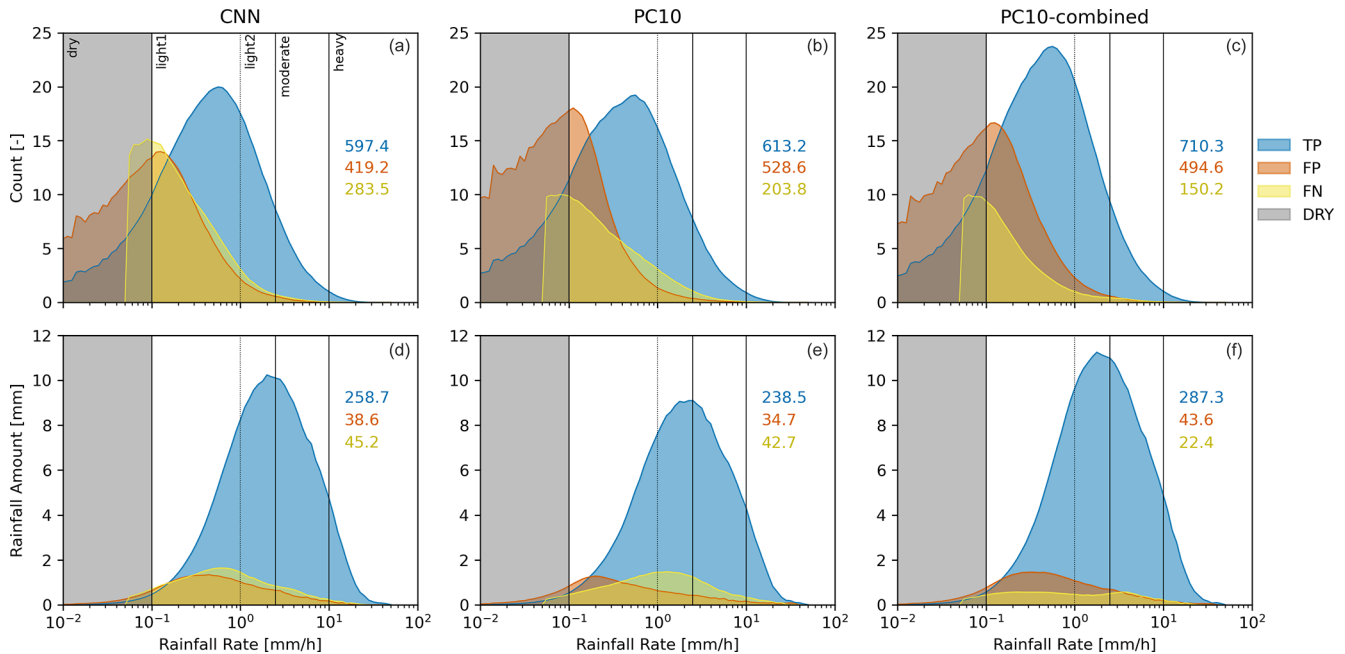
Figure 8. In panels **(a)**–**(c)**, the number of FP, TP, and FN time steps with a specific reference rain rate are compared for CNN **(a)**, PC10 **(b)**, and PC10-combined **(c)**. The respective amount of rainfall is shown in panels **(d)**–**(f)**. All quantities are an average per CML. The rain intensities for FP and TP are estimated by the CML, while the rain intensities for FN, where the CML rainfall rate is 0, are taken from the reference. The numbers in each panel are color-coded according to TP, FP, and FN and show the integrated amount for each curve.

5.2 Performance of a combination of TSB and ADB rain event detection methods compared to TSB-only and ADB-only methods

The combined method was able to outperform both pure ADB and TSB methods in detecting rain events. It was able to make a good trade-off between conservative and liberal methods used in the combination, which was shown by the superior MCC scores. Figure 6 illustrates how such an improvement can be achieved, for example, by reducing FNs that lead to a reset of the baseline at a higher level that ultimately leads to rainfall rates that are too small for PC10.

The choice of a starting method for the combination only had a small impact on the results because most, but not all, initial predictions are overwritten in the combination process. The best MCC and lowest bias were achieved by PC10-combined, which is why it was chosen for a more detailed comparison of scores for individual CMLs.

PC10-combined improved the MCC and PCC scores for the vast majority of all CMLs, and only single outliers achieved better scores using the pure ADB or TSB method. Thus, we conclude that the combination algorithm is robust against varying CML behavior. A limitation of the proposed combination is that CNN relies on 1 min instantaneously sampled CML data. However, a similar combination of ADB with other TSB methods that can handle, for example, the common 15 min "min–max" sampling should be easily applicable following the logic presented in Fig. 3.

5.3 Performance differences between day and night

We observed a notable classification performance drop during nighttime for PC and PC-Ph, but also for RS. For PC and PC-Ph this day and night difference is very likely due to the missing SEVIRI channels in the Vis range at night. The calculation of microphysical variables is mainly based on these channels. Their absence consequently limits the reliability of all derived precipitation products. According to Fig. 4, this effect significantly increases the rate of positive predictions.

While CNN was able to perform equally well during nighttime, the other TSB method RS showed a decreased performance. One possible explanation could be the formation of dew on the antennas during nighttime that can regularly be observed in CML time series as a slowly increasing (after sunset) and decreasing (after sunrise) attenuation. The more sophisticated pattern recognition algorithm of the CNN method seems to be able to correctly classify these periods as dry. The combined methods utilized the high confidence of the CNN and reduced the day and night difference.

However, the PCC results for PC and PC-Ph showed that a decrease in MCC during the night did not lead to a worse correlation of derived rainfall rates.

5.4 Performance for different rainfall intensity classes

Our results confirmed that the detection performance is much higher for moderate and heavy compared to light rainfall.
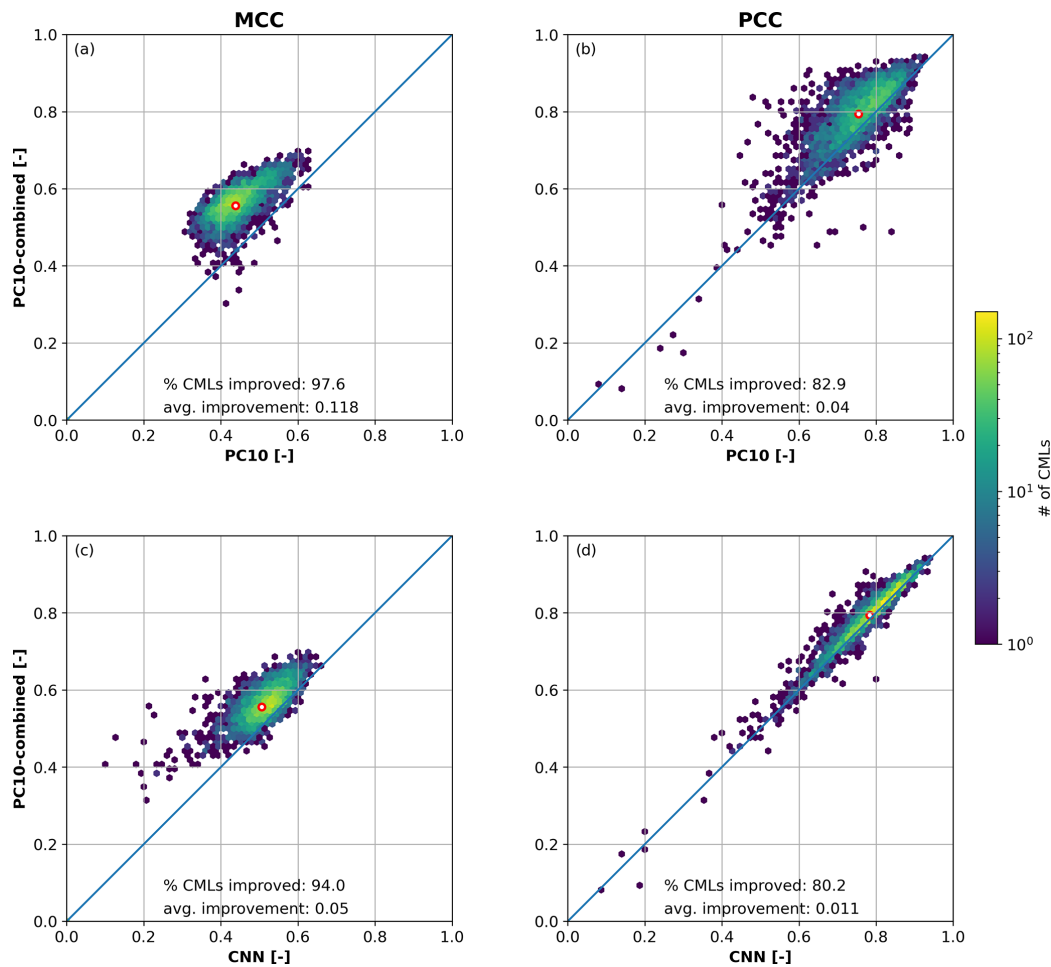
Figure 9. Scatter density comparison of the combination of ADB and TSB methods (PC10-combined) with pure ADB (PC10, **(a, b)**) and TSB (CNN, **(c, d)**) methods using the Matthews correlation coefficient (MCC, **(a, c)**) and the Pearson correlation coefficient (PCC, **(b, d)**). Each score is computed individually for each CML. The red point is the mean of the respective metrics of all CMLs per product.

This was already shown for TSB methods by Polz et al. (2020) and is now also confirmed for the ADB methods based on PC and PC-Ph. The TSB methods have to distinguish between rainfall signal and noise, which can become similar for low rainfall intensities. The ADB method using SEVIRI data suffers from its indirect measurement principle and may have difficulties in distinguishing between precipitation and non-precipitating clouds, particularly for light rain.

The contribution of the different intensity classes to the overall relative bias in Fig. 7 shows that the overestimation due to FPs in the dry class is smaller to the underestimation in the positive intensity classes where FNs are one major factor for missed rainfall. This way, all methods except PC01-combined show an overall negative bias. One additional explanation for the overall negative bias could be a compensation for WAA that is too large. Tiede et al. (2023) described strong WAA fluctuations during long-lasting rain events, a fact that is not considered in the WAA compensation method

we chose (or any other available method). Therefore, there is some uncertainty in WAA compensation, which influences the bias.

Although PC10 was more liberal, i.e., generally favoring positive predictions, the CNN was more confident in the prediction of heavy rainfall. The combined method increased the performance for low-rain-rate TPs compared to the TSB method because of the higher confidence of the ADB method with only a small increase in the count and rainfall amount through FPs. Therefore, we confidently claim that PC10-combined was able to improve the detection performance for the dry and for all positive intensity classes.

6 Conclusions

In this study, we aimed to address the questions of whether satellite-derived precipitation products are suitable indicators for rain event detection in CML data with respect to day/night differences and different rain intensities, and

whether combinations of TSB and ADB methods show an additional added value. We achieved this by using PC and PC-Ph from MSG SEVIRI in an ADB rain event detection and compared the results with two TSB rain event detection methods. Then, we combined the most promising variants in such a way that the most confident detection method was used for any given time step.

The results clearly show that PC and PC-Ph products from MSG SEVIRI can be used for the detection of rain events in CML attenuation time series. They performed almost as well as the TSB methods during daytime and worse than CNN during nighttime. Minor differences between the SEVIRI products PC and PC-Ph exist, but the chosen threshold of precipitation probability dominated the overall behavior. An improved PC-Ph product has been available since April 2022, potentially making its application in rain event detection even more attractive (Llorenç Lliso and José Alberto Lahuerta, NWC SAF, personal communication, 2023).

However, the performance of ADB methods based on SEVIRI was lower at night than during the day due to the lack of the three SEVIRI channels (Vis and NIR). Since CNN did not show a decrease in quality at night, it would be logical to vary the rain event detection for daytime and nighttime. We did not aim for such a temporal variation in order to avoid inconsistencies in the resulting time series. Compared to the ADB and CNN, the RS method does not show particular advantages, except for the easy application.

The quality of the rain event detection methods clearly depended on the rain intensity, with a better performance for moderate and heavy rain than for light rain. For flood forecasting, light rain is often negligible, but this is not the case for water balance analyses. Additionally, the increasing threat of droughts in the context of climate change also requires a high-quality representation of light rain. Low rainfall intensities show a large potential for improvement, and major differences in this study were also obtained there.

The effort to use ADB is greater than for TSB methods because the processing of additionally needed satellite data can be time-consuming. However, the global availability of the data allows for the unified processing of CML datasets from different countries and we assume that extensive re-calibration is not needed. Stepwise combinations with TSB methods that need to be adjusted to the characteristics of the CML data, as presented here, do need re-calibration and thus increase the effort. The additional improvements shown by the combinations are promising and justify the effort. There is a multitude of possibilities when combining different rain event detection methods. Using methods like the nearby-link approach or using different thresholds depending on data quality or rainfall intensity is also possible in future applications.

In principle, combinations of multiple TSB methods are possible and may lead to improvements. However, we recommend applying a combination of TSB and ADB methods to exploit the advantages of both approaches: TSB methods are easy to apply and provide precise results where the separation of noise and rainfall signals is obvious, whereas ADB methods show a better performance for noisy or unstable CML time series due to their independence of the actual CML signal. Burkina Faso, for example, has only a few rainfall stations but several hundred CMLs. Most CMLs outside the capital Ouagadougou are long (> 20 km) and use frequencies around 7 GHz. Their time series are quite noisy and show large fluctuations from sources other than rain. With abundant information from geostationary satellites and the methods presented in this work, we expect to extract useful ground-based rainfall information from such CMLs in this region with scarce rainfall data.

Appendix A: Additional figures

Algorithm 1
Combination of TSB and ADB methods. Example of CNN-PC-combined.

```
1: t ← CNN82
2: if PC01 is dry then
3:     t ← dry                    ▷ high confidence in dry predictions
4: if CNN94 is wet then
5:     t ← wet                    ▷ high confidence in wet predictions
6: if PC30 is wet then
7:     t ← wet                    ▷ high confidence in wet predictions
8: if CNN10 is dry then
9:     t ← dry                    ▷ high confidence in dry predictions
```

Figure A1. Algorithm describing the combination CNN–PC-combined of PC and CNN starting with CNN82. A given time step of CML data that needs to be processed is denoted by t. The different wet–dry methods give a wet or dry prediction for this time step as described in Sect. 3.1.1.

Appendix B: Additional tables

Table B1. Confusion matrix values TP, FP, TN, and FN as well as classification scores ACC and MCC and regression scores PCC and RB for all methods considered. For each metric the best score is written in bold font.

Group	Method	TP	FP	TN	FN	ACC	MCC	PCC	RB
Time series based (TSB)	RS	2 086 257	2 761 086	36 939 753	1 487 374	0.902	0.449	0.657	−0.165
	CNN	2 511 242	3 125 653	36 575 186	1 062 389	0.903	0.51	0.742	−0.115
Aux. data based (ADB)	PC01	3 103 560	7 412 469	32 288 370	470 071	0.818	0.438	0.73	−0.07
	PC10	2 809 793	5 525 566	34 175 273	763 838	0.855	0.452	0.707	−0.208
	PC20	2 100 523	3 258 161	36 442 678	1 473 108	0.891	0.423	0.636	−0.455
	PC30	1 136 635	1 205 697	38 495 142	2 436 996	0.916	0.35	0.509	−0.719
	PC–Ph01	2 860 243	6 112 184	33 588 655	**713 388**	0.842	0.439	0.731	−0.159
	PC–Ph10	2 029 703	2 703 467	36 997 372	1 543 928	0.902	0.441	0.689	−0.417
	PC–Ph20	1 376 271	1 408 014	38 292 825	2 197 360	0.917	0.392	0.637	−0.587
	PC–Ph30	893 173	**815 028**	**38 885 811**	2 680 458	**0.919**	0.324	0.58	−0.711
Combined	CNN–PC-combined	2 676 762	2 727 541	36 973 298	896 869	0.916	**0.566**	0.746	−0.108
	PC01-combined	**3 122 738**	4 379 019	35 321 820	450 893	0.888	0.555	0.742	0.026
	PC10-combined	3 010 509	3 762 008	35 938 831	563 122	0.9	**0.566**	0.743	−0.021
	CNN–PC-Ph-combined	2 529 058	2 588 598	37 112 241	1 044 573	0.916	0.548	**0.747**	−0.134
	PC–Ph01-combined	3 003 963	3 988 729	35 712 110	569 668	0.895	0.553	0.743	**−0.017**
	PC–Ph10-combined	2 656 801	2 865 316	36 835 523	916 830	0.913	0.554	0.746	−0.114

References

Atlas, D.: Radar in Meteorology – Battan Memorial and 40th Anniversary Radar Meteorology Conference, Boston, USA, 9–13 November 1987, Amer. Meteor. Soc., ISBN 0933876866, 1990.

Atlas, D. and Ulbrich, C. W.: Path- and Area-Integrated Rainfall Measurement by Microwave Attenuation in the 1–3 cm Band, J. Appl. Meteorol. Clim., 16, 1322–1331, https://doi.org/10.1175/1520-0450(1977)016<1322:PAAIRM>2.0.CO;2, 1977.

Bartels, H., Weigl, E., Reich, T., Lang, P., Wagner, A., Kohler, O., and Gerlach, N.: Projekt RADOLAN – Routineverfahren zur Online-Aneichung der Radarniederschlagsdaten mit Hilfe von automatischen Bodenniederschlagsstationen (Ombrometer), Deutscher Wetterdienst, Hydrometeorologie, https://www.dwd.de/DE/leistungen/radolan/radolan_info/home_abschlussbericht.html (last access: 28 July 2023), 2004.

Bruni, G., Reinoso, R., van de Giesen, N. C., Clemens, F. H. L. R., and ten Veldhuis, J. A. E.: On the sensitivity of urban hydrodynamic modelling to rainfall spatial and temporal resolution, Hydrol. Earth Syst. Sci., 19, 691–709, https://doi.org/10.5194/hess-19-691-2015, 2015.

Chwala, C. and Kunstmann, H.: Commercial microwave link networks for rainfall observation: Assessment of the current status and future challenges, WIREs Water, 6, e1337, https://doi.org/10.1002/wat2.1337, 2019.

Chwala, C., Gmeiner, A., Qiu, W., Hipp, S., Nienaber, D., Siart, U., Eibert, T., Pohl, M., Seltmann, J., Fritz, J., and Kunstmann, H.: Precipitation observation using microwave backhaul links in the alpine and pre-alpine region of Southern Germany, Hydrol. Earth Syst. Sci., 16, 2647–2661, https://doi.org/10.5194/hess-16-2647-2012, 2012.

Chwala, C., Keis, F., and Kunstmann, H.: Real-time data acquisition of commercial microwave link networks for hydrometeorological applications, Atmos. Meas. Tech., 9, 991–999, https://doi.org/10.5194/amt-9-991-2016, 2016.

Cristiano, E., ten Veldhuis, M.-C., and van de Giesen, N.: Spatial and temporal variability of rainfall and their effects on hydrological response in urban areas – a review, Hydrol. Earth Syst. Sci., 21, 3859–3878, https://doi.org/10.5194/hess-21-3859-2017, 2017.

D'Amico, M., Manzoni, A., and Solazzi, G. L.: Use of Operational Microwave Link Measurements for the Tomographic Reconstruction of 2-D Maps of Accumulated Rainfall, IEEE Geosci. Remote S., 13, 1827–1831, https://doi.org/10.1109/LGRS.2016.2614326, 2016.

Djibo, M., Chwala, C., Graf, M., Polz, J., Kunstmann, H., and Zougmoré, F.: High-resolution rainfall maps from commercial microwave links for a data-scarce region in West Africa, J. Hydrometeorol., 1, 1847–1861, https://doi.org/10.1175/JHM-D-23-0015.1, 2023.

DWD: Niederschlagsintensität, German Met. Service Glossary, German Meteorological Service, https://www.dwd.de/DE/service/lexikon/Functions/glossar.html?lv2=101812&lv3=101906, (last access: 28 July 2023), 2023a.

DWD: Index of /climate_environment/CDC/grids_germany/5_minutes/radolan/reproc/2017_002/, Deutscher Wetterdienst [data set], https://opendata.dwd.de/climate_environment/CDC/grids_germany/5_minutes/radolan/reproc/2017_002/ (last access: 28 July 2023), 2023b.

Fu, S., Sonnenborg, T. O., Jensen, K. H., and He, X.: Impact of Precipitation Spatial Resolution on the Hydrological Response of an Integrated Distributed Water Resources Model, Vadose Zone J., 10, 25–36, 2011.

Giannetti, F., Moretti, M., Reggiannini, R., and Vaccaro, A.: The NEFOCAST System for Detection and Estimation of Rainfall Fields by the Opportunistic Use of Broadcast Satellite Signals, IEEE Aero. El. Sys. Mag., 34, 16–27, https://doi.org/10.1109/MAES.2019.2916292, 2019.

Giro, R. A., Luini, L., Riva, C. G., Pimienta-del Valle, D., and Riera Salis, J. M.: Real-Time Rainfall Estimation Using Satellite Signals: Development and Assessment of a New Procedure, IEEE T. Instrum. Meas., 71, 1–10, https://doi.org/10.1109/TIM.2022.3165840, 2022.

Graf, M., Chwala, C., Polz, J., and Kunstmann, H.: Rainfall estimation from a German-wide commercial microwave link network: optimized processing and validation for 1 year of data, Hydrol. Earth Syst. Sci., 24, 2931–2950, https://doi.org/10.5194/hess-24-2931-2020, 2020.

Graf, M., El Hachem, A., Eisele, M., Seidel, J., Chwala, C., Kunstmann, H., and Bárdossy, A.: Rainfall estimates from opportunistic sensors in Germany across spatio-temporal scales, J. Hydrol.: Regional Studies, 37, 100883, https://doi.org/10.1016/j.ejrh.2021.100883, 2021.

Habi, H. V. and Messer, H.: Wet-Dry Classification Using LSTM and Commercial Microwave Links, in: 2018 IEEE 10th Sensor Array and Multichannel Signal Processing Workshop (SAM), 8–11 July 2018, Sheffield, UK, IEEE, 149–153, https://doi.org/10.1109/SAM.2018.8448679, 2018.

Haese, B., Hörning, S., Chwala, C., Bárdossy, A., Schalge, B., and Kunstmann, H.: Stochastic Reconstruction and Interpolation of Precipitation Fields Using Combined Information of Commercial Microwave Links and Rain Gauges, Water Resour. Res., 53, 10740–10756, https://doi.org/10.1002/2017WR021015, 2017.

Hernanz, A., Lahuerta García, J. A., Calbet, X., and Rípodas, P.: Algorithm Theoretical Basis Document for the Precipitation Product Processors of the NWC/GEO, NWCSAF, https://www.nwcsaf.org/Downloads/GEO/2021/Documents/Scientific_Docs/NWC-CDOP3-GEO-AEMET-SCI-ATBD-Precipitation_v1.0.1.pdf, (last access: 28 July 2023), 2019.

Hou, A. Y., Kakar, R. K., Neeck, S., Azarbarzin, A. A., Kummerow, C. D., Kojima, M., Oki, R., Nakamura, K., and Iguchi, T.: The Global Precipitation Measurement Mission, B. Am. Meteorol. Soc., 95, 701–722, 2014.

ITU-R: Specific attenuation model for rain for use in prediction methods (Recommendation P.838-3), ITU-R, https://www.itu.int/rec/R-REC-P.838-3-200503-I/en, (last access: 28 July 2023), 2005.

Kreklow, J., Tetzlaff, B., Burkhard, B., and Kuhnt, G.: Radar-Based Precipitation Climatology in Germany – Developments, Uncertainties and Potentials, Atmosphere, 11, 217, https://doi.org/10.3390/atmos11020217, 2020.

Kumah, K., Maathuis, B., Hoedjes, J., and Su, Z.: Near real-time estimation of high spatiotemporal resolution rainfall from cloud top properties of the MSG satellite and commercial microwave link rainfall intensities, Atmos. Res., 279, 106357, https://doi.org/10.1016/j.atmosres.2022.106357, 2022.

Kumah, K. K., Hoedjes, J. C. B., David, N., Maathuis, B. H. P., Gao, H. O., and Su, B. Z.: The MSG Technique: Improving Commercial Microwave Link Rainfall Intensity by Using Rain Area Detection from Meteosat Second Generation, Remote Sens., 13, 3274, https://doi.org/10.3390/rs13163274, 2021.

Lahuerta García, J. A.: Scientific and Validation Report for the Precipitation Product Processors of the NWC/GEO, Agencia Estatal de Meteorología, https://www.nwcsaf.org/AemetWebContents/ScientificDocumentation/Documentation/GEO/v2016/NWC-CDOP2-GEO-AEMET-SCI-VR-Precipitation_v1.0.pdf, (last access: 28 July 2023), 2019.

Lahuerta García, J. A.: Algorithm theoretical basis document for the precipitation product processors of the NWC/GEO, Agencia Estatal de Meteorología, https://www.nwcsaf.org/Downloads/GEO/2021/Documents/Scientific_Docs/NWC-CDOP3-GEO-AEMET-SCI-ATBD-Precipitation_v1.0.1.pdf, (last access: 28 July 2023), 2021.

Leijnse, H., Uijlenhoet, R., and Stricker, J. N. M.: Rainfall measurement using radio links from cellular communication networks, Water Resour. Res., 3, W03201, https://doi.org/10.1029/2006WR005631, 2007.

Leijnse, H., Uijlenhoet, R., and Stricker, J.: Microwave link rainfall estimation: Effects of link length and frequency, temporal sampling, power resolution, and wet antenna attenuation, Adv. Water Resour., 31, 1481–1493, https://doi.org/10.1016/j.advwatres.2008.03.004, 2008.

Liberman, Y., Samuels, R., Alpert, P., and Messer, H.: New algorithm for integration between wireless microwave sensor network and radar for improved rainfall measurement and mapping, Atmos. Meas. Tech., 7, 3549–3563, https://doi.org/10.5194/amt-7-3549-2014, 2014.

Maggioni, V., Meyers, P. C., and Robinson, M. D.: A Review of Merged High-Resolution Satellite Precipitation Product Accuracy during the Tropical Rainfall Measuring Mission (TRMM) Era, J. Hydrometeorol., 17, 1101–1117, https://doi.org/10.1175/JHM-D-15-0190.1, 2016.

Messer, H. and Sendik, O.: A New Approach to Precipitation Monitoring: A critical survey of existing technologies and challenges, IEEE Signal Proc. Mag., 32, 110–122, https://doi.org/10.1109/MSP.2014.2309705, 2015.

Messer, H., Zinevich, A., and Alpert, P.: Environmental Monitoring by Wireless Communication Networks, Science, 312, 713–713, https://doi.org/10.1126/science.1120034, 2006.

NWC SAF: PC and PC-Ph products, Nowcasting and Very Short Range Forecasting Satellite Application Facility (NWC SAF) [data set], https://www.nwcsaf.org/web/guest/nwc/geo-geostationary-near-real-time-v2021 (last access: 20 December 2023), 2023.

Overeem, A., Leijnse, H., and Uijlenhoet, R.: Measuring urban rainfall using microwave links from commercial cellular communication networks, Water Resour. Res., 47, W12505, https://doi.org/10.1029/2010WR010350, 2011.

Overeem, A., Leijnse, H., and Uijlenhoet, R.: Country-wide rainfall maps from cellular communication networks, P. Natl. Acad. Sci. USA, 110, 2741–2745, https://doi.org/10.1073/pnas.1217961110, 2013.

Overeem, A., Leijnse, H., and Uijlenhoet, R.: Two and a half years of country-wide rainfall maps using radio links from commer-

cial cellular telecommunication networks, Water Resour. Res., 52, 8039–8065, https://doi.org/10.1002/2016WR019412, 2016.

Pollock, M. D., O'Donnell, G., Quinn, P., Dutton, M., Black, A., Wilkinson, M. E., Colli, M., Stagnaro, M., Lanza, L. G., Lewis, E., Kilsby, C. G., and O'Connell, P. E.: Quantifying and Mitigating Wind-Induced Undercatch in Rainfall Measurements, Water Resour. Res., 54, 3863–3875, https://doi.org/10.1029/2017WR022421, 2018.

Polz, J., Chwala, C., Graf, M., and Kunstmann, H.: Rain event detection in commercial microwave link attenuation data using convolutional neural networks, Atmos. Meas. Tech., 13, 3835–3853, https://doi.org/10.5194/amt-13-3835-2020, 2020.

Rafieeinasab, A., Norouzi, A., Kim, S., Habibi, H., Nazari, B., Seo, D.-J., Lee, H., Cosgrove, B., and Cui, Z.: Toward high-resolution flash flood prediction in large urban areas – Analysis of sensitivity to spatiotemporal resolution of rainfall input and hydrologic modeling, J. Hydrol., 531, 370–388, https://doi.org/10.1016/j.jhydrol.2015.08.045, 2015.

Rios Gaona, M. F., Overeem, A., Leijnse, H., and Uijlenhoet, R.: Measurement and interpolation uncertainties in rainfall maps from cellular communication networks, Hydrol. Earth Syst. Sci., 19, 3571–3584, https://doi.org/10.5194/hess-19-3571-2015, 2015.

Roebeling, R. A. and Holleman, I.: SEVIRI rainfall retrieval and validation using weather radar observations, J. Geophys. Res.-Atmos., 114, D21202, https://doi.org/10.1029/2009JD012102, 2009.

Roebeling, R. A., Deneke, H. M., and Feijt, A. J.: Validation of Cloud Liquid Water Path Retrievals from SEVIRI Using One Year of CloudNET Observations, J. Appl. Meteorol. Clim., 47, 206–222, https://doi.org/10.1175/2007JAMC1661.1, 2008.

Roversi, G., Alberoni, P. P., Fornasiero, A., and Porcù, F.: Commercial microwave links as a tool for operational rainfall monitoring in Northern Italy, Atmos. Meas. Tech., 13, 5779–5797, https://doi.org/10.5194/amt-13-5779-2020, 2020.

Schleiss, M. and Berne, A.: Identification of Dry and Rainy Periods Using Telecommunication Microwave Links, IEEE Geosci. Remote S., 7, 611–615, https://doi.org/10.1109/LGRS.2010.2043052, 2010.

Schleiss, M., Olsson, J., Berg, P., Niemi, T., Kokkonen, T., Thorndahl, S., Nielsen, R., Ellerbæk Nielsen, J., Bozhinova, D., and Pulkkinen, S.: The accuracy of weather radar in heavy rain: a comparative study for Denmark, the Netherlands, Finland and Sweden, Hydrol. Earth Syst. Sci., 24, 3157–3188, https://doi.org/10.5194/hess-24-3157-2020, 2020.

Schmid, J.: The SEVIRI instrument, in: Proceedings of the 2000 EUMETSAT meteorological satellite data user's conference, Bologna, Italy, 29 May–2 June 2000, AEMET, vol. 29, 13–32, 2000.

Sevruk, B.: Rainfall Measurement: Gauges, Chap. 35, John Wiley & Sons, Ltd, ISBN 9780470848944, https://doi.org/10.1002/0470848944.hsa038, 2006.

Song, K., Liu, X., Zou, M., Zhou, D., Wu, H., and Ji, F.: Experimental Study of Detecting Rainfall Using Microwave Links: Classification of Wet and Dry Periods, IEEE J. Sel. Top. Appl., 13, 5264–5271, https://doi.org/10.1109/JSTARS.2020.3021555, 2020.

Steiner, M., Smith, J. A., and Uijlenhoet, R.: A Microphysical Interpretation of Radar Reflectivity-Rain Rate Relationships, J. Atmos. Sci., 61, 1114–1131, 2004.

Thoss, A.: Algorithm Theoretical Basis Document for Precipitating Clouds of the NWC/PPS, NWCSAF, https://www.nwcsaf.org/AemetWebContents/ScientificDocumentation/Documentation/PPS/v2014/NWC-CDOP2-PPS-SMHI-SCI-ATBD-4_v1_0.pdf, (last access: 28 July 2023), 2014.

Tiede, J., Chwala, C., and Siart, U.: New Insights Into the Dynamics of Wet Antenna Attenuation Based on In Situ Estimations Provided by the Dedicated Field Experiment ATTRRA2, IEEE Geosci. Remote S., 20, 1–5, https://doi.org/10.1109/LGRS.2023.3320755, 2023.

Uijlenhoet, R., Steiner, M., and Smith, J. A.: Variability of Raindrop Size Distributions in a Squall Line and Implications for Radar Rainfall Estimation, J. Hydrometeor., 4, 43–61, 2003.

Uijlenhoet, R., Overeem, A., and Leijnse, H.: Opportunistic remote sensing of rainfall using microwave links from cellular communication networks, WIREs Water, 5, e1289, https://doi.org/10.1002/wat2.1289, 2018.

UNFCCC: Sharm el-Sheikh Implementation Plan, Revised draft decision-/CMA.4, UNFCCC, https://unfccc.int/documents/621908 (last access: 12 April 2024), 2022.

van de Beek, R. (C. Z.)., Olsson, J., and Andersson, J.: Optimal grid resolution for precipitation maps from commercial microwave link networks, Adv. Sci. Res., 17, 79–85, https://doi.org/10.5194/asr-17-79-2020, 2020.

van het Schip, T. I., Overeem, A., Leijnse, H., Uijlenhoet, R., Meirink, J. F., and van Delden, A. J.: Rainfall measurement using cell phone links: classification of wet and dry periods using geostationary satellites, Hydrolog. Sci. J., 62, 1343–1353, https://doi.org/10.1080/02626667.2017.1329588, 2017.

Villarini, G. and Krajewski, W. F.: Review of the Different Sources of Uncertainty in Single Polarization Radar-Based Estimates of Rainfall, Surv. Geophys., 31, 107–129, https://doi.org/10.1007/s10712-009-9079-x, 2010.

Wagner, A.: Spatiotemporal Variability of Precipitation: Measurements – Simulations – Limitations, doctoralthesis, Universität Augsburg, https://opus.bibliothek.uni-augsburg.de/opus4/files/38014/Wagner_Diss.pdf, (last access: 28 July 2023), 2018.

Wagner, A., Seltmann, J., and Kunstmann, H.: Joint statistical correction of clutters, spokes and beam height for a radar derived precipitation climatology in southern Germany, Hydrol. Earth Syst. Sci., 16, 4101–4117, https://doi.org/10.5194/hess-16-4101-2012, 2012.

Wang, Z., Schleiss, M., Jaffrain, J., Berne, A., and Rieckermann, J.: Using Markov switching models to infer dry and rainy periods from telecommunication microwave link signals, Atmos. Meas. Tech., 5, 1847–1859, https://doi.org/10.5194/amt-5-1847-2012, 2012.

Winterrath, T., Rosenow, W., and Weigl, E.: On the DWD quantitative precipitation analysis and nowcasting system for real-time application in German flood risk management, Weather Radar and Hydrology, IAHS Publ. 351, 323–329, https://www.dwd.de/DE/leistungen/radolan/radolan_info/Winterrath_German_flood_risk_management_pdf.html?blob=publicationFile&v=4 (last access: 28 July 2023), 2012.

Winterrath, T., Brendel, C., Hafer, M., Junghänel, T., Klameth, A., Lengfeld, K., Walawender, E., Weigl, E., and Becker, A.: RADKLIM Version 2017.002: Reprocessed quasi gauge-adjusted radar data, 5-minute precipitation sums (YW), Deutscher Wetterdienst (DWD), https://doi.org/10.5676/DWD/RADKLIM_YW_V2017.002, 2018.